

Wigner crystallization in quantum wires within the Yukawa approximation

Reyna Méndez-Camacho,^{1,*} Esteban Cruz-Hernández,¹ and Ramón Castañeda-Priego^{2,†}

¹*Coordinación para la Innovación y Aplicación de la Ciencia y la Tecnología, Universidad Autónoma de San Luis Potosí, Sierra Leona 550, 78210, S.L.P., Mexico*

²*División de Ciencias e Ingenierías, Campus León, Universidad de Guanajuato, Loma del Bosque 103, 37150, León, Mexico*
(Received 21 September 2016; revised manuscript received 6 January 2017; published 28 February 2017)

One crucial and important aspect to account for the nature of the quantum wires is the understanding of the effects associated to many-body interactions between confined electrons. The inclusion of such many-body forces in any theoretical framework is a difficult and computationally demanding task. Then one has to make use of coarse-grained descriptions that allow one to incorporate the contribution of all the electrons. In a simple physical picture, the interaction between two electrons can be considered screened due to the presence of the other ones. If the latter are homogeneously distributed inside the wire, the interaction between the former can then be assumed of the Yukawa form. In this contribution, we report on the lower energy states of n -doped GaAs circular-quantum wires with two electrons in the conduction band interacting through a repulsive Yukawa potential. By varying the length and the electronic density of the wire, quite different trends in the electronic distribution are observed. By changing the material parameters to InSb and InAs nanowires, we found that our results are consistent with available experimental data that have reported the formation of Wigner crystals.

DOI: [10.1103/PhysRevB.95.085437](https://doi.org/10.1103/PhysRevB.95.085437)

I. INTRODUCTION

Technological progress in the epitaxial fabrication of semiconductor quantum wires (QWRs) by diverse growth techniques, such as molecular beam epitaxy (MBE) and metal-organic chemical-vapor deposition, have allowed the synthesis of high-quality QWRs of different materials and geometries [1,2]. QWRs possess unique one-dimensional (1D) quantum confinement properties and have emerged as promising structures for the next generation of electronic and optoelectronic devices, for example, photodetectors, solar cells, field-effect transistors, light-emitting diodes, or low-threshold lasers [3–7]. In addition, the strong 1D confinement of electrical carriers, photons, and phonons makes the QWRs very attractive laboratory systems for probing 1D physics of great interest both experimentally and theoretically [8–13] in condensed matter.

Parallel to the experimental advance in the fabrication and characterization of QWRs, a vigorous theoretical modeling area has been developed with an increasing level of sophistication that, nowadays, allows us to gain a deeper understanding of the physical properties of QWRs. Theoretical predictions have shown that the electron-electron (e - e) interactions in 1D electron systems are unique and of importance to account for interesting phenomena. For example, Wigner crystallization is one of the most remarkable many-body effects in 1D systems where electrons spontaneously form a self-organized lattice [14]. The formation of such 1D electronic structure has been predicted by using some complex models, see, e.g., Refs. [13,15–17], and, recently, some experimental signatures of a Wigner crystal have been reported [8–10].

Several studies addressing the single-electron confinement in QWRs of different geometries have been investigated using tight-binding and effective bond-orbital models, as well as classical envelope function schemes like the parabolic

band approximation (PBA), the Luttinger model, and the eight-band k - p model [18–21]. On the other hand, the many-body correlations that emerge due to e - e interactions in QWRs have been reported during the last few years within the effective field theory, Hartree-Fock, and the density functional theory approaches [8,12,22–26]. In general, such approaches involve large computational times and complex mathematical calculations when many-body forces are explicitly included and only short wires [elongated quantum dots (QDs)], containing a small number of electrons, have been considered. Furthermore, due to the inherent difficulty of these models to address the many-body effects and to deal with long QWRs, critical values for the electronic concentration and QWR length required to observe the Wigner crystallization phenomenon remains unclear.

One way to overcome the inherent difficulties that arise when many-body interactions are incorporated into the description of QWRs is the use of coarse-grained potentials that are able to capture the effects of many-body forces. In particular, the use of Yukawa-like potentials to address the many-body problem has been extensively used in other branches of physics, such as soft matter [27] and nuclear physics [7]. Surprisingly, the problem of two electrons in a QWR, as far as we know, has not been systematically studied by using a repulsive Yukawa potential even when, at least qualitatively, many experimentally observed trends can be reproduced with this potential model that considers a pair of pointlike particles interacting via a screened Coulomb potential. For instance, in a recent contribution, the screening effects on the binding energy of a neutral donor in parabolic QWRs were studied and authors derived a modified Yukawa potential that takes into account the contribution of the parabolic confining potential [28]. Furthermore, it has been recently shown that the interaction between a pair of electrons in a quasi-one-dimensional electron gas embedded in a semiconductor cylindrical QWR has a Yukawa functional form [29].

The aim of this work is to numerically solve the Schrödinger equation for two nonrelativistic electrons without spin con-

*reyna.mendez@uaslp.mx

†ramoncp@fisica.ugto.mx

fined in circular QWRs of infinite barriers interacting effectively through a Yukawa-like potential. The electronic distribution into the wire is studied as a function of the electronic density (n) and the length of the wire (L). By varying the screening parameter κ in the Yukawa potential, electronic densities ranging from the bare Coulomb regimen (just two electrons) to high-doped GaAs QWRs are analyzed. The length L of the wire is varied from 10 nm (into the regimen of QD confinement) up to 10 μm (very long wires).

II. THEORETICAL APPROXIMATION

A. Two-electron system: Schrödinger equation and Yukawa potential

The time-independent Schrödinger equation for the two-electron wave function Ψ_{e_1, e_2} is given by:

$$-\frac{\hbar^2}{2m_e^*} \sum_{i=1}^2 \nabla_i^2 \Psi_{e_1, e_2} + V_{\text{eff}} \Psi_{e_1, e_2} = E \Psi_{e_1, e_2}, \quad (1)$$

where $\hbar \equiv h/2\pi$, h is the Planck constant, m_e^* is the electron effective mass, $\Psi_{e_1, e_2} \equiv \Psi((\varrho_1, \theta_1, z_1), (\varrho_2, \theta_2, z_2))$ and $V_{\text{eff}} = V_{e-w}(\varrho, \theta) + V_Y(r)$ is the total interaction potential, which contains the electron-wall (e-w) interaction, V_{e-w} , in the transversal confined ρ - θ plane, which is zero inside the QWR and infinite outside, and the longitudinal e - e Yukawa-like interaction (V_Y), which has the form [27],

$$V_Y(r) = \frac{e^2}{4\pi\epsilon\epsilon_0} \frac{\exp[-\kappa r]}{r}, \quad (2)$$

where r is the electron-electron separation distance, e is the electron charge, ϵ the dielectric constant of the QWR, ϵ_0 the vacuum permittivity, and the screening parameter κ is given by

$$\kappa = \sqrt{\frac{2e^2 n}{\epsilon_0 \epsilon k_B T}}, \quad (3)$$

with n the electronic density, k_B the Boltzmann constant, and T the temperature. For simplicity, we will consider that the pair of electrons are located along the z axis (Fig. 1), so that their relative distance r along the wire is now $z_1 - z_2$ and $V_Y(r)$ reduces to $V_Y(z)$.

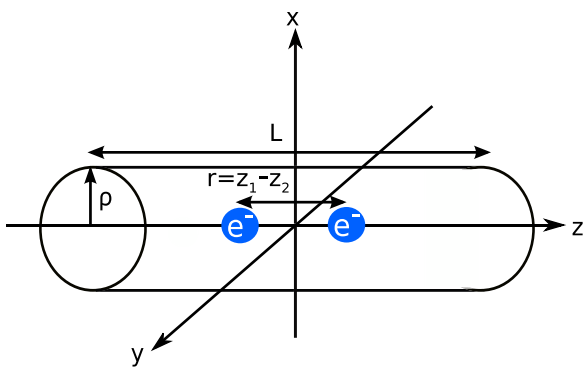


FIG. 1. Schematic representation of two electrons located in a cylindrical quantum wire. For convenience, electrons are placed along the z axis at $(0, 0, z_1)$ and $(0, 0, z_2)$.

In order to solve Eq. (1), it is convenient to rewrite it in a simpler form by using the position of the center of mass $R = \frac{z_1 + z_2}{2}$ and the reduced mass $\mu = \frac{m^*}{2}$. Then, by using

$$z_1 = R + \frac{r}{2}, \quad (4)$$

$$z_2 = R - \frac{r}{2}, \quad (5)$$

one can redefine the nabla operators in terms of the coordinates r and R as

$$\nabla_1 = \nabla_r + \frac{1}{2} \nabla_R, \quad (6)$$

$$\nabla_2 = -\nabla_r + \frac{1}{2} \nabla_R. \quad (7)$$

Thus, Eq. (1) can be reexpressed as

$$\left[-\frac{\hbar^2}{4m_e^*} \nabla_R^2 - \frac{\hbar^2}{2\mu} \nabla_r^2 + V_{\text{eff}}(r) \right] \Psi_{e_1, e_2} = E \Psi_{e_1, e_2}. \quad (8)$$

Equation (8) has two contributions: one that depends only on the center of mass of the two-particle system (R) and the other that is only a function of the relative distance between the electrons (r). By setting $\Psi_{e_1, e_2} = A(r)B(R)$, one can rewrite Eq. (8) as

$$\left[-\frac{\hbar^2}{4m_e^* B} \nabla_R^2 B(R) \right] - \left[\frac{\hbar^2}{2\mu A(r)} \nabla_r^2 A - V_{\text{eff}}(r) \right] = E, \quad (9)$$

where $E = E_R + E_r$ contains two independent contributions. The solution of Eq. (1) can be then reduced to the solution of two simpler and independent equations, namely,

$$-\frac{\hbar^2}{4m_e^*} \nabla_R^2 B(R) = E_R B(R), \quad (10)$$

$$-\frac{\hbar^2}{2\mu} \nabla_r^2 A(r) + V_{\text{eff}}(r) A(r) = E_r A(r). \quad (11)$$

Equation (10) corresponds to a particle of mass $2m_e^*$ at the center of the QWR, confined in the ϱ - θ plane, and free to move in the z axis. By choosing $B(R) = F_1(\varrho_R)F_2(\theta_R)F_3(z_R)$, the solutions in the center of mass of Eq. (10) are given by

$$F_1(\varrho_R) = J_\alpha(\varrho_R), \quad (12)$$

$$F_2(\theta_R) = e^{ip\theta_R}, \quad (13)$$

$$F_3(z_R) = f_1 \sin(\beta z_R) + f_2 \cos(\beta z_R), \quad (14)$$

with $E_R = E_{\varrho_R} + E_{\theta_R} + E_{z_R}$, $J_\alpha(\varrho_R)$ the Bessel functions of order α , $\beta^2 = 4m_e^* E_{z_R} / \hbar^2$ and f_1, f_2 constant terms. With the boundary condition $J_\alpha(\varrho_R = \rho) = 0$, the eigenenergies $E_{l\varrho_R}$ become $E_{l\varrho_R} = \frac{\hbar^2 C_{p,l}^2}{4m_e^* \rho^2}$, where $C_{p,l}$ are the zeros of the Bessel function with $l = 1, 2, \dots$ and $p = 0$ due to radial symmetry. Using the boundary conditions $F_3(z_R = \pm L/2) = 0$, the eigenenergies E_{nz_R} become $E_{nz_R} = \frac{\hbar^2 n^2 \pi^2}{4m_e^* L^2}$ and $E_{n(n+1)z_R} = \frac{\hbar^2 n^2 (n+1)^2 \pi^2}{m_e^* L^2}$ for the even and the odd solutions, respectively, with $n = 1, 2, \dots$. In this work, we consider $\alpha = 1$ and $C_{0,1} = 2.4048$, which corresponds to the first zero of the Bessel function and is associated to the cross-sectional ground state.

On the other hand, Eq. (11) corresponds to a particle of reduced mass μ moving under the potential V_{eff} . As infinite

barriers are explicitly considered, this potential possesses only the contribution of the Yukawa potential [Eq. (2)] along the QWR. Equation (11) is numerically solved in a uniform grid by using the finite differences method [30] with a bin size $\Delta r = 10^{-6}L/2$ and employing the following boundary conditions $A(r = \pm L/2) = 0$ and $A(r = 10^{-6}) = 1$. In the Appendix, the accuracy of the numerical solution of Eq. (11) is tested in the case of the unconfined two-electron system.

B. Semiconductor quantum wires

In this work, free-standing circular GaAs QWRs of cross sectional ratio $\rho = 4$ nm and L ranging from 10 nm to 10 μ m are considered. The natural length and energy scales are given by the Bohr radius, $a_B = \epsilon\hbar^2/m_e^*e^2$, and twice the Rydberg energy, $2E_{Ry} = \hbar^2/m_e^*a_B^2$, respectively. For GaAs at a temperature (T) of 300 K, these parameters take the values: $a_B = 10.26$ nm and $2E_{Ry} = 10.78$ meV, with $\epsilon = 12.9$ and $m_e^* = 0.0665m_e$ (m_e the electron mass). The screening parameter is set to $\kappa_C = 10^{-6} \text{ nm}^{-1}$, $\kappa_D = 1 \text{ nm}^{-1}$, $\kappa_{HD} = 100 \text{ nm}^{-1}$, and $\kappa_{UD} = 5000 \text{ nm}^{-1}$, which correspond, via Eq. (3), to electron densities of $n_C = 10^6 \text{ cm}^{-3}$ (covering the range of intrinsic and bare Coulombic interaction), $n_D = 10^{18} \text{ cm}^{-3}$ (doped GaAs), $n_{HD} = 10^{22} \text{ cm}^{-3}$ (highly-doped GaAs), and $n_{UD} = 10^{25} \text{ cm}^{-3}$ (experimentally unachievable doping level [31]), respectively. Our model focuses on direct wide band-gap semiconductor compounds, then the small interaction between conduction and valence bands is neglected in the calculations. The model is easily applicable to other wide band-gap compounds, for example, for free standing InSb QWRs the parameters should be modified according to the following values: $m_e^* = 0.014m_e$, $\epsilon = 16.8$, $a_B(\text{InSb}) = 63.469$ nm, and $2E_{Ry}(\text{InSb}) = 1.338$ meV. Analogously, for free standing InAs QWRs, $m_e^* = 0.023m_e$, $\epsilon = 15.15$, $a_B(\text{InAs}) = 34.845$ nm, and $2E_{Ry}(\text{InAs}) = 2.711$ meV.

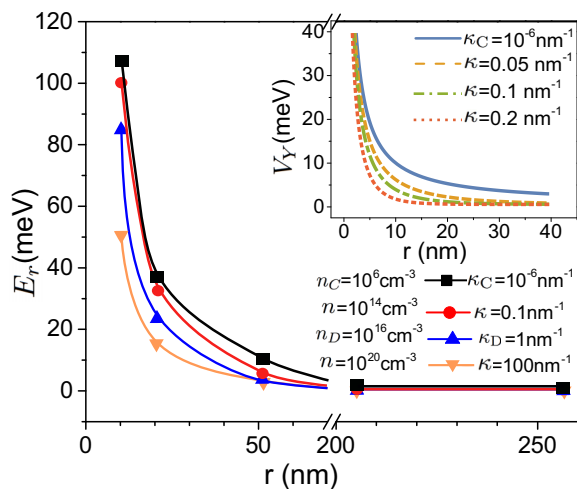


FIG. 2. Electron-electron interaction as a function of the interparticle separation for different values of the electronic density n . Inset shows the Yukawa potential contribution to $V_{\text{eff}}(r)$.

III. RESULTS AND DISCUSSION

A. Screening effects

In Fig. 2, the energy E_r (V_{eff} plus the kinetic energy) as a function of the electron separation for different electronic concentrations is displayed. As expected, the $e-e$ interaction energy is weaker when the carrier density increases as a consequence of the enhancement of the screening effect. The screening effect is specially noticeable when the $e-e$ distance is below 50 nm. For a short separation (< 10 nm), the $e-e$ potential changes from ~ 107 meV for $\kappa_C = 10^{-6} \text{ nm}^{-1}$ to ~ 50.5 meV for $\kappa_{HD} = 100 \text{ nm}^{-1}$, reducing the energy in ~ 56.5 meV. On the other hand, for a large separation (200 nm) and for the same values of κ , the energy changes only in ~ 1.06 meV. For an $e-e$ separation above 200 nm, the $e-e$ energy is practically zero and independent of the screening parameter. The inset in Fig. 2 shows the functional form of $V_Y(z)$. Strictly speaking, the bare Coulomb potential is recovered when $\kappa = 0$, however, for the wire lengths used in this work, this condition is virtually equivalent to $\kappa_C = 10^{-6} \text{ nm}^{-1}$.

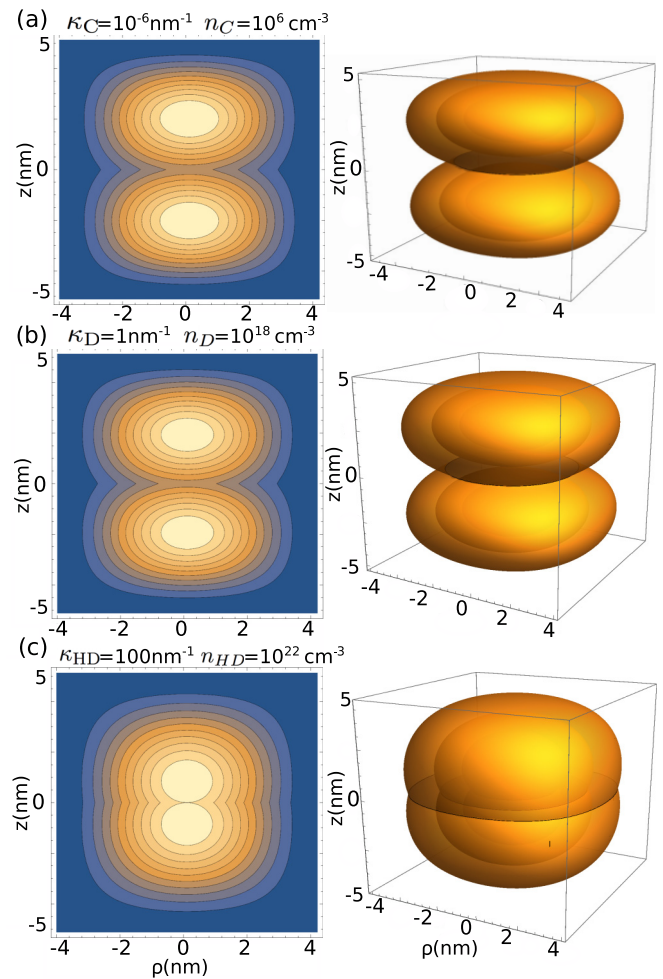


FIG. 3. 2D and 3D projections of $|A(z)|^2$ for the ground state, taken along the axis of the QWR, for different electronic concentrations, $\rho = 4$ nm and $L = 10$ nm.

B. Transversal and longitudinal electronic distribution

For QWRs ($L > 80$ nm), the electronic confinement in the transversal direction (ϱ - θ plane) is much stronger than the confinement in the longitudinal direction (ϱ - z plane). Thus, one can consider that the system in the transversal direction will remain in the ground state and that the excited states will be those arising from the weak confined (longitudinal) z direction. Due to the nature of our model and the position of the e - e pair, the transversal states are exactly those obtained from a single electron confined in a circular quantum well of infinite barriers (which is not dependent on the length or the extrinsic carrier concentration of the QWR). This is a

well-known problem [32], therefore, we here do not provide information of the well-known one-body problem.

The ϱ - z (2D) projections of the electronic density $|A(z)|^2$ for the ground state of 10-nm-long QWRs with different carrier concentrations are shown on the left side of Fig. 3. The right side shows the corresponding 3D projections, which display additional details of the electronic distribution. As observed in the ground state, the electrons exhibit twofold symmetric distributions which, due to the screening effect, can be overlapped when the electronic density is increased. From this dependence, one obtains valuable information of the electronic distribution in the limits of long and high doped wires in a simple way.

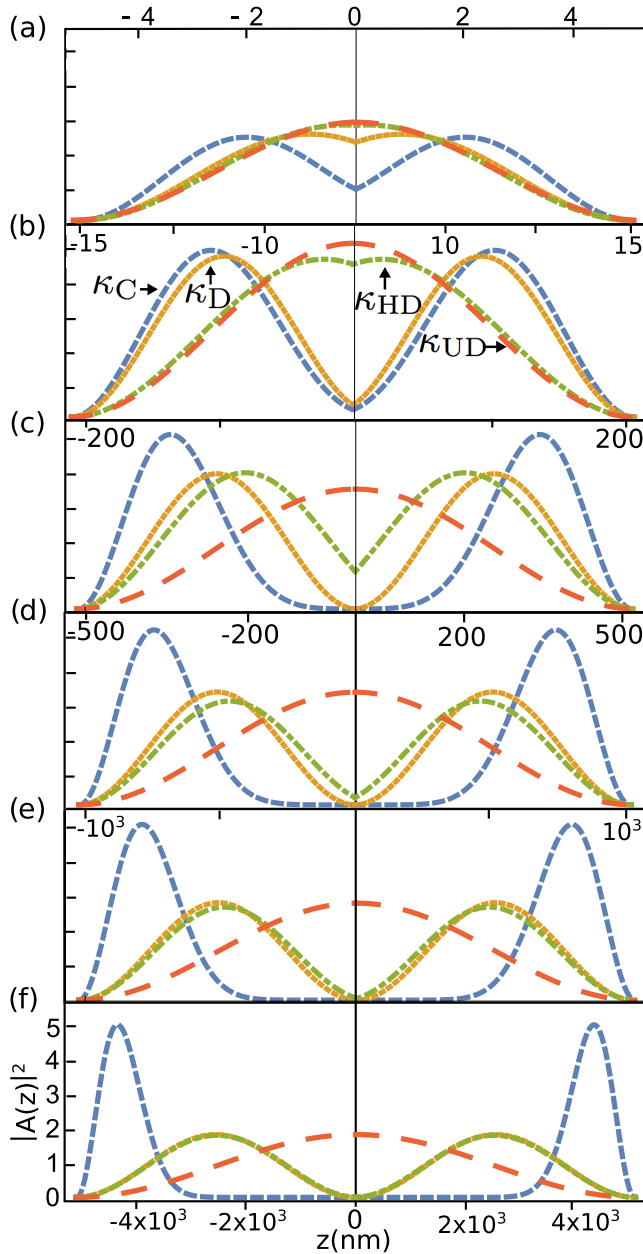


FIG. 4. Ground state probability profiles, $|A(z)|^2$, along the z axis, for $\kappa_C = 10^{-6} \text{ nm}^{-1}$, $\kappa_D = 1 \text{ nm}^{-1}$, $\kappa_{HD} = 100 \text{ nm}^{-1}$, and $\kappa_{UD} = 5000 \text{ nm}^{-1}$, for different lengths of the wire: (a) 10 nm, (b) 30 nm, (c) 400 nm, (d) 1 μm , (e) 2 μm , and (f) 10 μm .

C. Wigner crystallization in the ground state

We now turn our discussion to the formation of a Wigner crystal. Despite the simplicity of our model, it can be used to analyze the many-body 1D interacting system under a number of different scenarios by an easy-to-do modification in variables such as the e - e separation, the electronic density, and the QWR length. In Fig. 4, the profiles of the ground state electronic densities $|A(z)|^2$, taken along the z axis, are presented for six different wire lengths. The values of L were chosen to cover the threshold between quantum-dot-like and effective QWR-like confinement (for GaAs, $L_{th} \sim 80$ nm). The electronic density was varied from 10^6 cm^{-3} (for κ_C) to 10^{22} cm^{-3} (for κ_{HD}) to cover the experimental achievable electronic concentrations. Additionally, an unfeasible high concentration of 10^{25} cm^{-3} (for κ_{UD}) has also been considered to explore this limit.

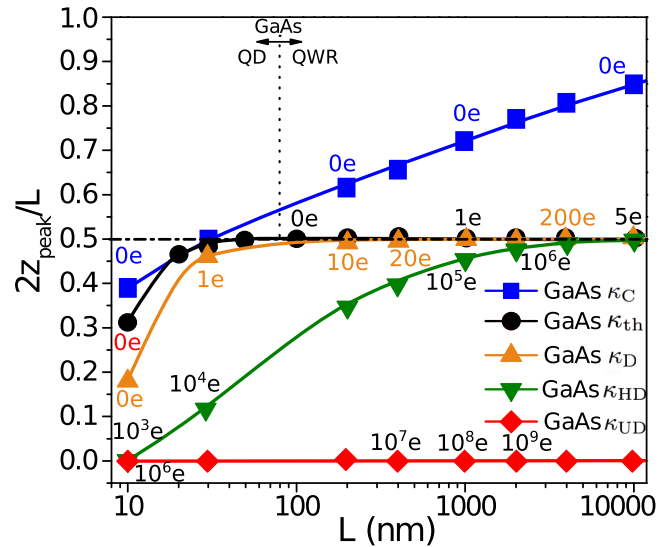


FIG. 5. Peak position, $2z_{\text{peak}}/L$, of the electronic distribution presented in Fig. 4. The approximated charge added by κ , in units of the electron charge, are presented for some representative wire lengths. The horizontal line represents the condition for Wigner localization. The vertical line defines the transition from QD-like to QWR-like confinement as established by the minimal electronic concentration (given for GaAs by $\kappa_{th} = 10^{-1} \text{ nm}^{-1}$) that allows Wigner localization.

For the lowest value of κ_C , the electronic density added by the Yukawa component (10^6 cm^{-3}) is practically zero for all the wire lengths here considered. Therefore, for κ_C the two electrons can be considered as interacting by a bare Coulomb potential, which in turn forces the two electronic distributions to be as separated as possible. The latter behavior is better observed in Fig. 5, where the position, $2z_{\text{peak}}/L$, of the center of one of the peaks of the distributions in Fig. 4 is plotted as a function of the QWR length for different electronic concentrations. In Fig. 5, the approximately electronic charge (in units of the electron charge) added by each value of κ for different wire lengths is shown.

For κ_C , the pair of electrons interact without any additional electronic charge, therefore, the interparticle spacing increases in a progressive way, not affected by the transition length L_{th} , i.e., from QD-like confinement to the regimen of an effective QWR-like confinement. In contrast, for κ_D , in the regimen of strong QD confinement, the very small extra charge (which is a fraction of the electron charge) is able to produce a screening effect that provokes that the electrons remain closer than for the case of κ_C . Even more, in remarked contrast with the case of κ_C ,

when the length of the wire is longer than 400 nm, an electronic distribution, characterized by two perfectly independent peaks and localized at $\pm L/4$, is established, so defining the formation of a Wigner molecule [14–17]. A similar behavior is observed for κ_{HD} with the difference that the Wigner localization is completely established for a longer wire length ($\sim 10 \mu\text{m}$). In contrast, for a quite high electronic concentration (κ_{UD}), the electronic interaction is completely screened even for very long wires. Therefore, in this last case the charge distribution remains centered at the origin as a unique maximum, impeding the Wigner crystallization formation.

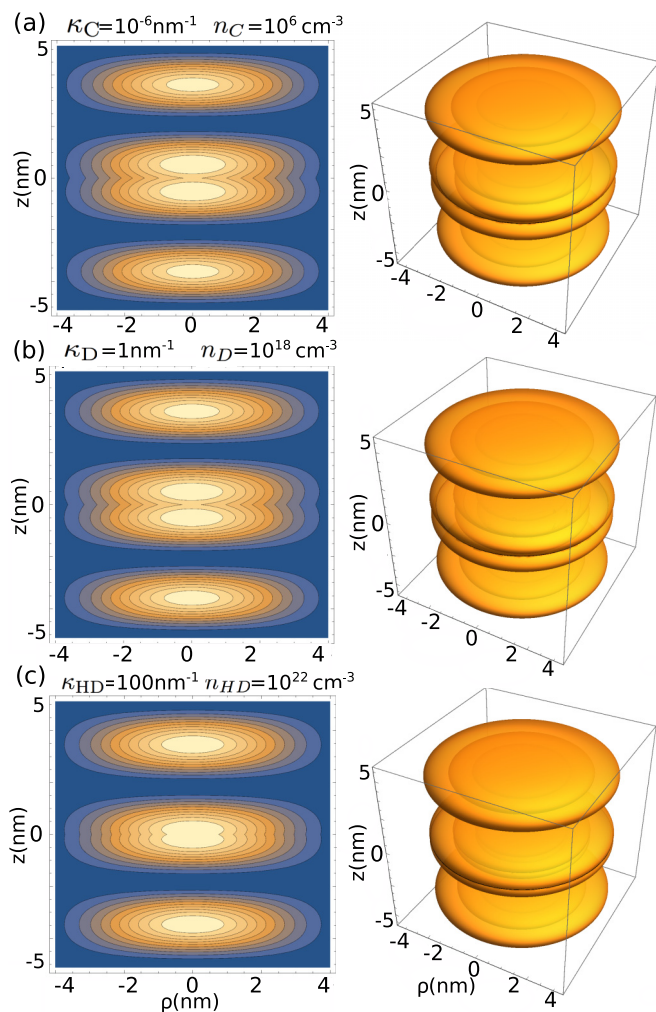


FIG. 6. 2D and 3D projection of the probability density $|A(z)|^2$ for the first excited state, taken along the z axis, for different values of the screening parameter, with $\rho = 4 \text{ nm}$ and $L = 10 \text{ nm}$.

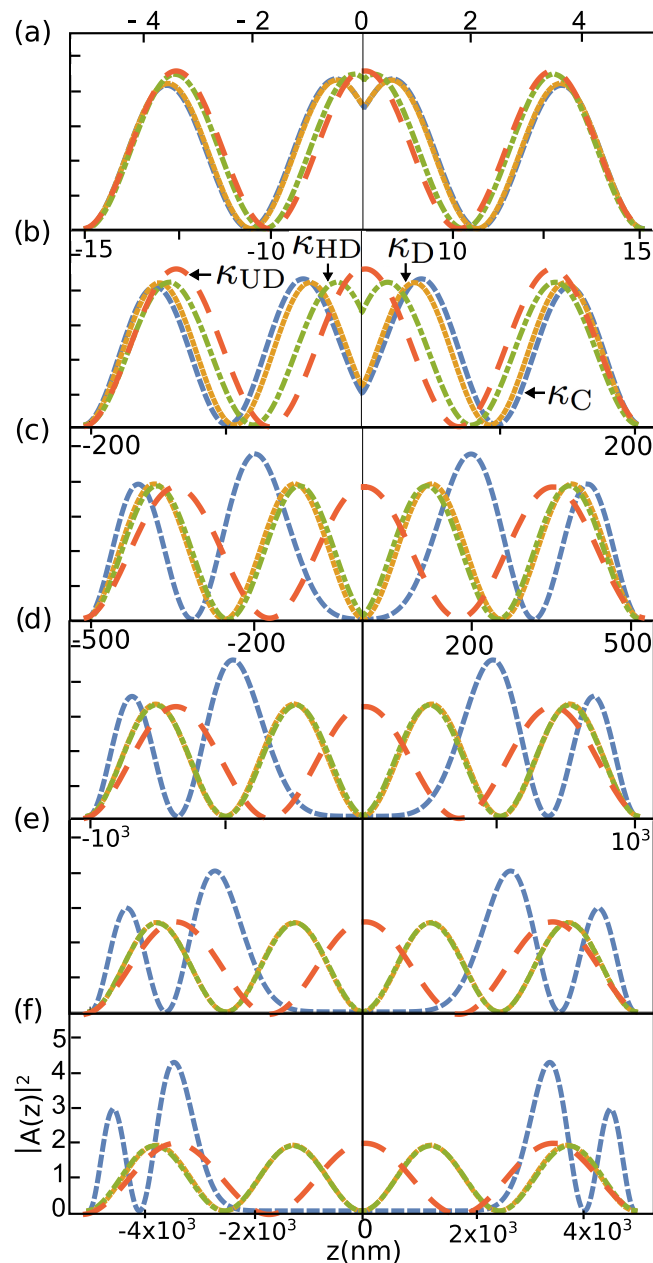


FIG. 7. Probability density, $|A(z)|^2$, for the first excited state for $\kappa_C = 10^{-6} \text{ nm}^{-1}$, $\kappa_D = 1 \text{ nm}^{-1}$, $\kappa_{HD} = 100 \text{ nm}^{-1}$, and $\kappa_{UD} = 5000 \text{ nm}^{-1}$; for different lengths of the wire: (a) 10 nm, (b) 30 nm, (c) 400 nm, (d) 1 μm , (e) 2 μm , and (f) 10 μm .

D. Wigner crystallization in excited states

The simplicity of our model also permits the straightforward examination of the excited states along the weak confined z direction, which in turns allow us to obtain additional information of the Wigner molecule formation in the excited states. The 2D and 3D projections in the plane ϱ - z of the electronic density $|A(z)|^2$ for the first excited state of 10 nm-long QWRs with different carrier concentrations are shown in Fig. 6. In Fig. 7, the corresponding profiles of the electronic densities $|A(z)|^2$ of the first excited state displayed in Fig. 6, along the z axis, are presented for different wire lengths. We observe that for realistic doping levels, a fourfold distribution is established. The trend can be observed more clearly in Fig. 8, where the center position of one of the maximal peaks of the electronic distribution is plotted as a function of the wire length. The positions for the peak

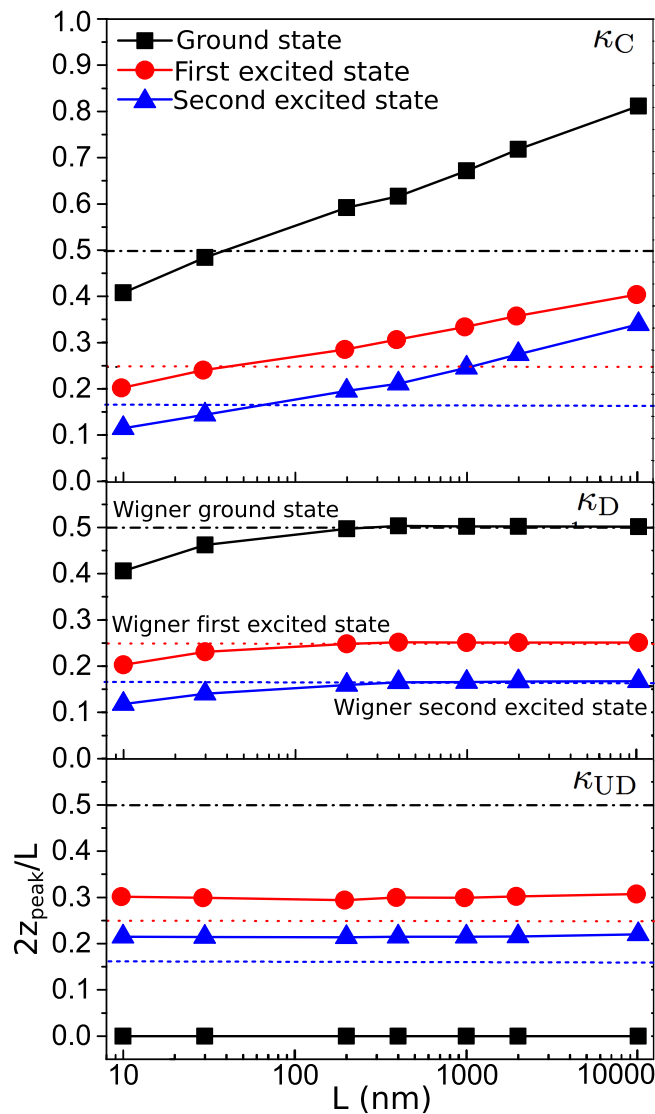


FIG. 8. Peak position, $2z_{\text{peak}}/L$, of the electronic distribution $|A(z)|^2$ presented in Fig. 7 for the lower energy states of the QWRs at different electronic concentrations as a function of the wire length. The horizontal lines represent the Wigner localization condition for the ground and the two first excited states.

equidistant distribution (when the Wigner crystal is formed) are displayed by horizontal lines in Fig. 8 for the ground, first, and second excited states. We observe that for the electronic concentrations from zero to 10^6 cm^{-3} (Coulombic regimen) and the unachievable large doping levels around 10^{25} cm^{-3} or larger, the Wigner crystal cannot be established. In the first case, the peak distributions move away from the center as the length increases and, in the second case, the distribution is “frozen” at an almost constant position independently of the wire length. In contrast, for electronic concentration in the range of 10^7 cm^{-3} to 10^{22} cm^{-3} (moderate and highly doped levels), similarly to the ground state, the electronic distributions establish a Wigner crystal when the length of the wire reaches a critical value. This critical length is almost the same for the three states, however, it can be observed that for more energetic states larger lengths are needed to completely reach the Wigner crystal formation.

E. Comparison with available experimental results

We contrast our model with experimental data reporting the formation of the Wigner molecule in InSb [8] and InAs [9] semiconductor nanowires. In order to make a direct comparison, in Fig. 9 the parameters of our model were properly changed to match the reported experimental conditions for InSb ($\kappa_{\text{InSb}} = 0.5 \text{ nm}^{-1}$) and InAs ($n_{\text{InAs}} = 10^{17} \text{ cm}^{-3}$). In Ref. [8], experimental tunneling spectroscopy measurements of electron localized states in epitaxially grown InSb nanowires are reported. Their results show the onset of Wigner localization for 160 nm wires and a theoretical prediction of complete Wigner localization in a 300 nm long InSb wire, which contains between two and three electrons. As observed from Fig. 9, our results match remarkable well with the latter values; the experimental data are marked by the vertical arrows. On the other hand, in Ref. [9] the local

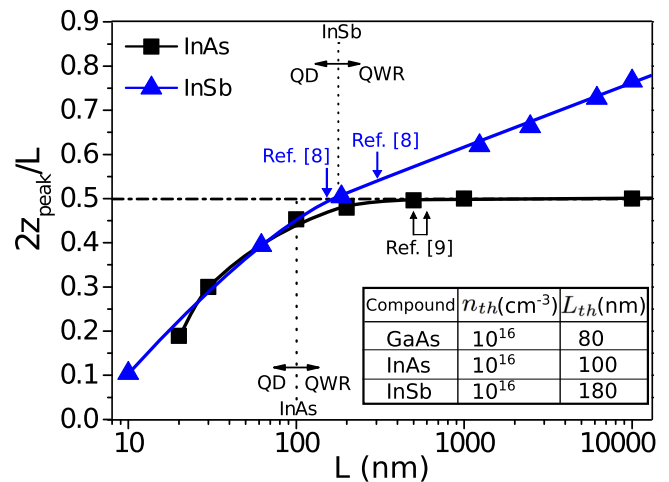


FIG. 9. Peak position, $2z_{\text{peak}}/L$, of the ground state electronic distribution, $|A(z)|^2$, for InSb and InAs QWR as a function of the wire length. The electronic concentrations were set to match the corresponding Refs. [8] and [9]. The vertical lines define the threshold length (L_{th}) from QD-like to QWR-like confinement for the two types of wires. Inset displays the values of n_{th} and L_{th} for the different types of wires.

electronic transport by scanning gate microscopy measurements of epitaxially grown InAs nanowires is reported. In the latter, the Wigner crystal formation is reported for wire lengths between 500 and 600 nm. As observed from Fig. 9, our results also reproduce correctly the reported experimental values. Finally, it is worth noting that apparently in the InSb wires, due to the very low electronic concentration, the Wigner condition is not reached because the electronic interaction is basically of Coulombic nature, again in good agreement with our theoretical predictions discussed above.

IV. CONCLUDING REMARKS

In this work, we have introduced a Yukawa model that allowed us to take into account the many-electron problem into a quantum wire of circular cross section of variable length and extrinsic doping level in a simple way. We used the Yukawa model to study the ground and excited states of a two-electron system confined in a quantum wire. Additionally, within this approximation, we were able to explore, in a simplified way, some new features of the Wigner molecule formation in a systematic manner. By establishing critical electronic densities and wire lengths, our model showed density correlations of a nearly perfect 1D Wigner crystal that are fully consistent with experimental reports. We should point out that our model is especially well adapted to study many-electron interactions (up to realistic levels of 10^{24} cm^{-3}) and very long QWRs ($> 10 \mu\text{m}$).

Last, but not least, we should stress that in this contribution we studied the particular case of GaAs quantum wires, nonetheless, our approximation can be straightforwardly applied to study the Wigner crystal formation in other systems, such as coupled systems of QDs and QWRs, or the transport phenomenon of electronic carriers when an external electric field is applied. Work along these lines is in progress.

ACKNOWLEDGMENTS

Authors acknowledge partial financial support from Conacyt (Grants No. 257434 and No. 237425). R.C.-P. acknowledges the financial support provided by Conacyt through a sabbatical Grant (Convocatorias 2016 de Estancias Sabáticas al Extranjero) and the Marcos Moshinsky fellowship 2013-2014. R.C.-P. also acknowledges The NIST Center for Neutron Research (Gaithersburg, MD) for hosting his sabbatical leave during the period September 2016–August 2017.

APPENDIX : UNCONFINED TWO-ELECTRON SYSTEM

To test the accuracy of the algorithm for the numerical solution of Eq. (11), we first evaluate the wave functions of

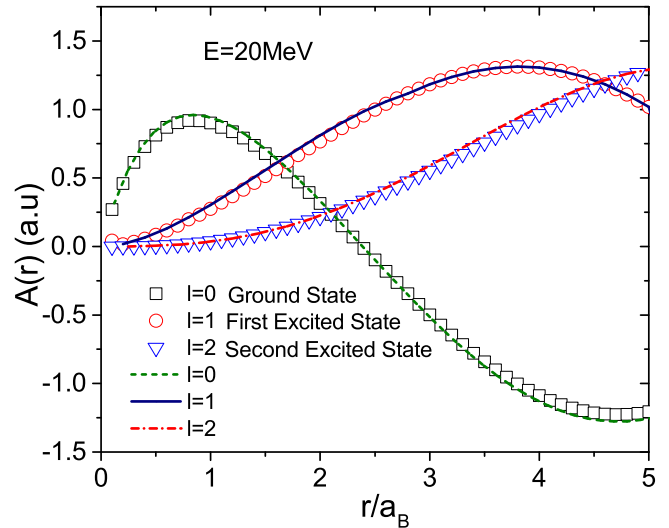


FIG. 10. Wave functions as a function of the e - e separation for the ground, first, and second excited states for a two-electron system in the continuum. The symbols represent the numerical data reported in Ref. [33]. The lines are obtained by solving numerically Eq. (11) by means of the finite difference method and using the parameters reported in Ref. [33] with $E_r = 20 \text{ MeV}$.

two particles in the continuum (nonconfined conditions, $\rho \gg 1 \text{ nm}$) interacting with the Yukawa potential given by:

$$V_Y(r) = C \frac{\exp[-r/r_0]}{r/r_0}, \quad (\text{A1})$$

with C a prefactor, $r_0 = 1.35 \times 10^{-13}$, and r the radial component [33]. Equation (10) is solved in spherical coordinates. The radial equation takes the form

$$-\frac{\hbar^2}{2\mu} \frac{1}{r^2} \frac{d}{dr} \left(r^2 \frac{dA(r)}{dr} \right) + \left(V_Y + \frac{l(l+1)}{r^2} \right) A(r) = E_r A(r), \quad (\text{A2})$$

with $l = 0, 1$, and 2 for the ground, first, and second excited state, respectively, $E_r = 20 \text{ MeV}$, $L_r^* = 5$ (in reduced units) and the boundary conditions $A(r = 10^{-6}) = 1/L$, $A'(r = 10^{-6}) = 0$. The numerical results are explicitly compared with those reported in Ref. [33] for the ground state, first, and second excited states, see Fig. 10.

Additionally, the algorithm was tested for the solution of Eq. (11) when the screening parameter takes the value $\kappa \rightarrow \infty$, i.e., in the limit of free electrons for the Yukawa potential of Eq. (2). For high electron densities, $n \sim 10^{28} \text{ cm}^{-3}$, a single charge distribution localized in the center of the QWR is obtained, that is, the free-electron limit is recovered (data not shown).

[1] Y. Xia, P. Yang, Y. Sun, Y. Wu, B. Mayers, B. Gates, Y. Yin, F. Kim, and H. Yan, *Adv. Mater.* **15**, 353 (2003).

[2] E. Cruz-Hernández, S. Shimomura, and V. H. Méndez-García, *Appl. Phys. Lett.* **101**, 073112 (2012).

[3] W. Wei, X.-Y. Bao, C. Soci, Y. Ding, Z.-L. Wang, and D. Wang, *Nano Lett.* **9**, 2926 (2009).

[4] R. R. LaPierre, A. C. E. Chia, S. J. Gibson, C. M. Haapamaki, J. Boulanger, R. Yee, P. Kuyanov, J. Zhang, N. Tajik, N. Jewell *et al.*, *Phys. Status Solidi RRL* **7**, 815 (2013).

- [5] Y. Cui, Z. Zhong, D. Wang, W. U. Wang, and C. M. Lieber, *Nano Lett.* **3**, 149 (2003).
- [6] D. M. Ethan, F. Kelkensberg, M. van Kouwen, J. A. van Dam, L. P. Kouwenhoven, V. Zwiller, M. T. Borgström, O. Wunnicke, M. A. Verheijen, and E. P. A. M. Bakkers, *Nano Lett.* **7**, 367 (2007).
- [7] B. Hua, J. Motohisa, Y. Kobayashi, S. Hara, and T. Fukui, *Nano Lett.* **9**, 112 (2009).
- [8] L. H. Kristinsdóttir, J. C. Cremon, H. A. Nilsson, H. Q. Xu, L. Samuelson, H. Linke, A. Wacker, and S. M. Reimann (Nanometer Structure Consortium, nmC@LU), *Phys. Rev. B* **83**, 041101(R) (2011).
- [9] A. A. Zhukov, C. Volk, A. Winden, H. Hardtdegen, and T. Schäpers, *JETP Lett.* **100**, 32 (2014).
- [10] V. D. Vikram and B. Marc, *Nat. Phys.* **4**, 314 (2008).
- [11] N. T. Ziani, F. Cavaliere, and M. Sassetti, *New J. Phys.* **15**, 063002 (2013).
- [12] G. A. Fiete, J. Qian, Y. Tserkovnyak, and B. I. Halperin, *Phys. Rev. B* **72**, 045315 (2005).
- [13] S. A. Söfving, M. Bortz, I. Schneider, A. Struck, M. Fleischhauer, and S. Eggert, *Phys. Rev. B* **79**, 195114 (2009).
- [14] E. Wigner, *Phys. Rev.* **46**, 1002 (1934).
- [15] J. S. Meyer and K. A. Matveev, *J. Phys. Condens. Matter* **21**, 023203 (2009).
- [16] H. J. Schulz, *Phys. Rev. Lett.* **71**, 1864 (1993).
- [17] J.-J. Wang, W. Li, S. Chen, G. Xianlong, M. Rontani, and M. Polini, *Phys. Rev. B* **86**, 075110 (2012).
- [18] M. Luisier, A. Schenk, W. Fichtner, and G. Klimeck, *Phys. Rev. B* **74**, 205323 (2006).
- [19] D. S. Citrin and Y. C. Chang, *IEEE J. Quantum Electron.* **29**, 97 (1993).
- [20] B. Trauzettel, I. Safi, F. Dolcini, and H. Grabert, *Phys. Rev. Lett.* **92**, 226405 (2004).
- [21] V. V. Ravi Kishore, B. Partoens, and F. M. Peeters, *Phys. Rev. B* **82**, 235425 (2010).
- [22] G. Sun and T. Vekua, *Phys. Rev. B* **93**, 205137 (2016).
- [23] D. S. Kosov and J. C. Greer, *Phys. Lett. A* **291**, 46 (2001).
- [24] J. I. Climente, M. Royo, J. L. Movilla, and J. Planelles, *Phys. Rev. B* **79**, 161301(R) (2009).
- [25] J. Planelles, M. Royo, A. Ballester, and M. Pi, *Phys. Rev. B* **80**, 045324 (2009).
- [26] A. Ballester, J. M. Escartín, J. L. Movilla, M. Pi, and J. Planelles, *Phys. Rev. B* **82**, 115405 (2010).
- [27] L. F. Rojas-Ochoa, R. Castañeda-Priego, V. Lobaskin, A. Stradner, F. Scheffold, and P. Schurtenberger, *Phys. Rev. Lett.* **100**, 178304 (2008).
- [28] Y. Wang, W.-D. Miao, and L.-X. Zhai, *Phys. Lett. A* **378**, 442 (2014).
- [29] K. H. Aharonyan and N. B. Margaryan, *J. Phys.: Conf. Ser.* **672**, 012009 (2016).
- [30] W. H. Press, S. A. Teukolsky, W. T. Vetterling, and B. P. Flannery, *Numerical Recipes in C (2nd ed.): The Art of Scientific Computing* (Cambridge University Press, New York, 1992).
- [31] D. R. Khanal, J. W. L. Yim, W. Walukiewicz, and J. Wu, *Nano Lett.* **7**, 1186 (2007).
- [32] H. Paul, *Quantum Wells, Wires and Dots: Theoretical and Computational Physics of Semiconductor Nanostructures* (John Wiley and Sons, England, 2006), 2nd ed.
- [33] W. Fetterman, E. Osborne, and D. S. Saxon, *J. Res. Natl. Bur. Stand.* **52**, 259 (1953).